Nanoscale

PAPER

View Article Online
View Journal | View Issue

Cite this: *Nanoscale*, 2017, **9**, 11187

Electrodeposited high strength, thermally stable spectrally selective rhenium nickel inverse opals†

Runyu Zhang,[a,b,c] Joseph Cohen,[a] Shanhui Fan[d] and Paul V. Braun *[a,b,c,e]

Rhenium–Nickel (Re_xNi_{100-x}) based 3D metallic inverse opals (IOs) were realized *via* colloidal crystal templated electrodeposition from an aqueous electrolyte. By varying the electrodeposition parameters, *x* could be varied from 0 to 88. Under reducing conditions, the rhenium-rich IOs were structurally stable to temperatures of at least 1000 °C for 5 h and for at least 12 h after coating with a thin layer of Al_2O_3. This demonstrated level of thermal stability is significantly improved compared to previously reported electrodeposited refractory inverse opals with similar characteristic dimensions. A strong frequency dependence in the optical reflection, which ranged from ~5% around 1.5 μm to ~65% around 5 μm, is predicted by simulations and experimentally observed, indicating the potential of this structure as a high temperature spectrally selective optical absorber/emitter. The elastic modulus of the ReNi IO structure is ~35 GPa and the hardness is ~0.8 GPa. Both these properties are much higher than those of Ni inverse opals and other periodically porous materials with similar characteristic pore dimensions. We suggest this work provides a promising approach for thermally stable mesostructured materials for high temperature catalyst supports, refractory photonics and mechanical applications including high temperature filtration, and high temperature actuators.

Received 18th May 2017,
Accepted 14th July 2017

DOI: 10.1039/c7nr03567e

rsc.li/nanoscale

Introduction

Metal foams produced by bubbling gas or adding foaming agents into molten metals generally contain wide distributions of pore diameters.[1–3] Motivating fabrication of foams with narrow pore size distributions, it has now been shown that porous materials composed of very well controlled networks of interconnecting hierarchical structures can exhibit properties far different than their bulk counterparts.[4,5] Through approaches which couple colloidal self-assembly, holographic lithography, and two photon direct laser writing with various material growth strategies,[6–9] three-dimensionally microstructured materials with interesting properties for applications in energy absorption,[10] electrochemical energy storage,[11–14] catalysis,[15,16] and filtration[17] have been realized. When the solids volume fraction in such structures is low, the general results are materials that can exhibit density-mass relationships not available in solid materials.[4] When the characteristic dimensions are on the order of about a micron or less, and the structure is appropriately designed, three dimensionally microstructured metals can also exhibit novel photonic properties, *e.g.*, frequency selective light absorption and thermal emission[14,18–20] or strong plasmonic responses.[21] For a number of both photonic and non-photonic applications, *e.g.*, thermophotovoltaics[22–25] and catalysis, long-term operation under extremely high temperature (*i.e.* >1000 °C) can be required. All except the most refractory foams will sinter and collapse under these conditions, which has led for these applications to a focus on microstructured conductive structures formed from tungsten (W),[25,26] tantalum (Ta),[24] carbon (C)[27,28] and electrically conductive ceramics.[25,29] For example, 3D tungsten (W) inverse opals made using atomic layer deposition (ALD) showed stability up to 1400 °C once coated with a thin ceramic coating.[25] Compared to ALD, electroplating is more scalable, can be used to deposit a wider range of pure metals, metal alloys,[30,31] and semiconductors[15,30,32] without the need of vacuum processing. Electroplating can also be performed under aqueous conditions compatible with many classes of templates.[7,15] We and others have reported the electroplating of both W and Ta from high temperature molten salt or ionic liquid baths,[26,33] with the attempts to structure those materials into complex geometries, however the resulting

[a]*Department of Materials Science and Engineering, University of Illinois at Urbana Champaign, Urbana, IL, 61801, USA. E-mail: pbraun@illinois.edu*
[b]*Frederick Seitz Materials Research Laboratory, University of Illinois at Urbana Champaign, Urbana, IL, 61801, USA*
[c]*Beckman Institute of Advanced Science and Technology, University of Illinois at Urbana Champaign, Urbana, IL, 61801, USA*
[d]*Department of Electrical Engineering, Stanford University, Stanford, California, 94305, USA*
[e]*Department of Chemistry, University of Illinois at Urbana Champaign, Urbana, IL, 61801, USA*

†Electronic supplementary information (ESI) available. See DOI: 10.1039/c7nr03567e

structures did not exhibit the expected high temperature stability, and the high temperature of the plating process was experimentally challenging.[26] The fact that a high temperature non-aqueous electrolyte was required undesirably reduces the list of template materials (for example, a polymer template formed *via* direct later writing would be difficult to use). It should also be noted that W and Ta are vulnerable to oxidation at high temperatures even under reducing atmospheres, due to their thermodynamically strongly favored oxide state.[34,35]

Here we focus on electroplated rhenium (Re) structures. Re is a near noble transition metal which possesses the third highest melting temperature of all elements, a high modulus of elasticity, superior tensile strength, large creep-rupture strength, and is ductile between subzero and high temperatures.[36,37] Unlike W and Ta, Re does not readily oxidize in reducing atmospheres.[38] Due to these properties, Re has found use in jet engines and rockets,[39] and as a catalyst for reforming.[40] While pure Re is difficult to electroplate from aqueous solutions, due to its redox potential being close to the hydrogen evolution potential,[36] co-plating of Re with transition group metal elements (Ni, Fe, Co) from low temperature aqueous baths has been shown for thin films with compositions up to 97 at% Re.[41,42] These works provided mechanistic studies of electrochemically-induced Re deposition, but no material properties or potential applications have been reported for electrochemically grown Re-rich alloys. Here, we report for the first time the formation and properties of three-dimensionally structured ReNi inverse opals using electrodeposition through self-assembled opal templates. These structures exhibit superior thermal stability relative to previously reported electroplated 3D metallic structures, frequency-selective reflection in the near infrared (NIR) spectrum and a higher mechanical strength and hardness than previously reported inverse opals.

Results and discussion

Discussions on electroplating ReNi alloy thin films, the plating mechanism, and alloying with other transition group metals can be found in literature,[41,42] and served as the starting point for this work. The fabrication scheme for the ReNi structures is shown in Fig. 1a and discussed in details in the experimental methods. First, PS colloid-based 3D sacrificial templates are self-assembled on a conductive substrate. Samples are then placed in the plating solutions and held at a constant electric potential. The deposited alloy fills the interstitials of the stacked spheres, forming a continuous network. After sacrificial template removal, the resulting structure consists of a network of close-packed air spheres in a metal matrix. Fig. 1b shows a SEM cross-sectional image of a half-filled opal template on a gold coated glass substrate, deposited from a pH 6 aqueous electrolyte consisting of 93 mM NH_4ReO_4, 93 mM $Ni(SO_3NH_2)_2$, and 343 mM citric acid. The interface between the filled and non-filled opal regions is smooth and flat, in distinct contrast with the rough films observed in the literature for template-free growth of similarly thick films.[41] This reduction in roughness of electrodeposited films due to the template is something we have observed in many systems. A few small cracks are detected in the cross-sectional images, perhaps caused by the hydrogen evolution during the electrodeposition. It has previously been shown that hydrogen can both accumulate and penetrate into plated metals and result in cracking due to hydrogen embrittlement.[43] The close-packed air

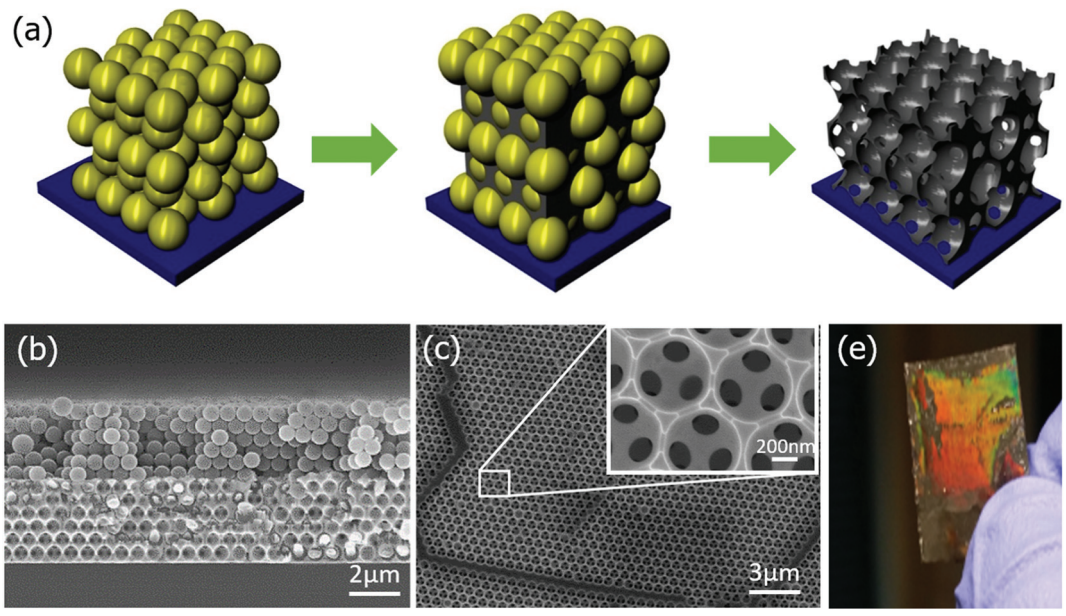

Fig. 1 (a) Schematic for the ReNi inverse opal fabrication process. (b) SEM cross section of a $Re_{88}Ni_{12}$ half-filled opal template and (c) SEM large area and higher magnification (inset) top-view of an $Re_{88}Ni_{12}$ inverse opal. (d) Optical image of a $Re_{88}Ni_{12}$ inverse opal on a W substrate.

spheres observed after the removal of the PS spheres (Fig. 1c) closely matches the initial size and arrangement of the spheres. The inset shows the surface of the as-deposited ReNi inverse opal is smooth with no visible grain structure. Strong coloration is observed in the optical image (Fig. 1e) due to light scattering from the surface which is textured with features with sizes comparable to the wavelength of visible light.

EDX spectroscopy (Fig. 2a) is collected from a sample deposited using the recipe described above. Both the Re M peak (1.842 keV) and Lα peak (8.651 keV) as well as Ni L_α and K_α peaks (0.851 keV and 7.477 keV, respectively) are clearly observed. Inductively coupled plasma atomic emission spectroscopy (ICP) indicates the sample is 88 at% Re and 12 at% Ni (this sample will be referred to as $Re_{88}Ni_{12}$). XRD was collected from samples on the W substrates before and after annealing at 700 °C (Fig. 2b). After annealing for 5 h at 700 °C, multiple peaks at positions similar but offset to a small degree for both hcp Re and hcp Ni are observed. Based on the ICDD reference cards 04-001-0055 (Re, hcp) and 01-089-7129 (Ni, hcp), we surmise the co-deposited Re and Ni forms a hcp solid solution with peaks offset from both pure Re and pure Ni. Based on Vegard's law, using the lattice parameters of hcp Re and Ni, we estimate the composition of the electrodeposited material to be ~87 at% Re, matching closely the ICP results. A strong W (200) peak, along with a (211) peak, are also detected, indicating that the W substrates are polycrystalline, but mostly (200) oriented. In contrast with after annealing, in the as-deposited sample, neither Re nor Ni peaks are observed in XRD, and only a diffuse hump is observed, suggesting that the material is either amorphous, or very small grain.

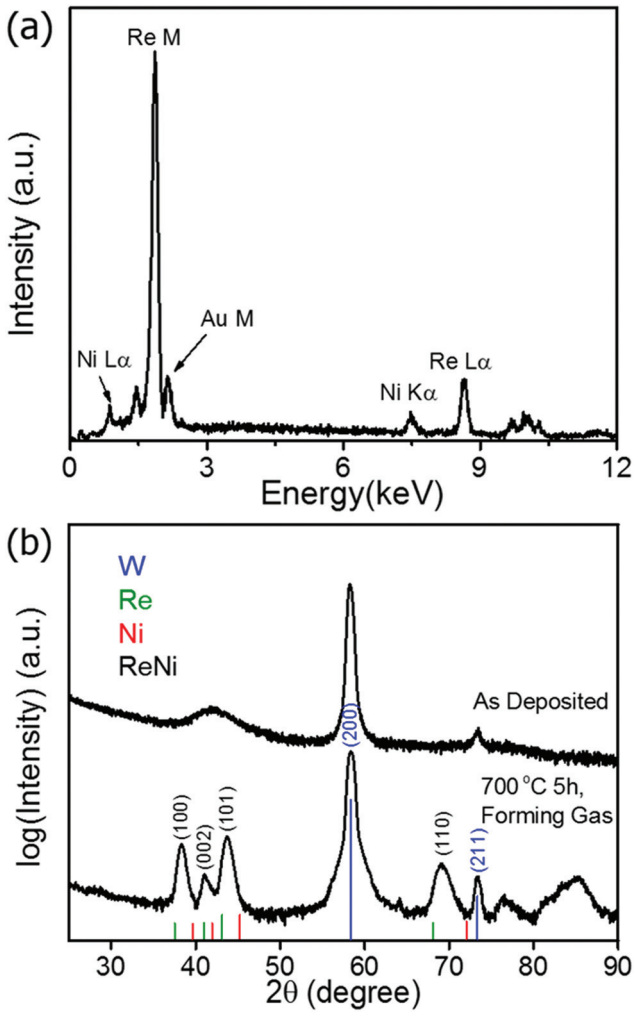

Fig. 2 (a) EDX spectrum for $Re_{88}Ni_{12}$ sample deposited on an Au coated glass substrate and (b) XRD spectra for a sample deposited on W before and after annealing at 700 °C. W (blue), Re (green), Ni (red), and ReNi (black) peak positions are labeled.

The thermal stability of samples with different compositions were investigated. First pure Ni, $Re_{55}Ni_{45}$, and $Re_{88}Ni_{12}$ were investigated. SEM images of each sample after annealing at 700 °C for 1 h are shown in Fig. 3a–c. It is clear Re enhances the thermal stability. After annealing, the microstructure of the Ni IO drastically degrades while the $Re_{88}Ni_{12}$ scaffold shows almost no change other than the emergence of small cracks on the surface. The $Re_{55}Ni_{45}$ scaffold shows an interesting behavior. After annealing, an intact, but rough scaffold with particles scattered throughout the structure is observed. This morphology is perhaps caused by phase separation into a Re-rich phase and a Ni rich phase,[44] with the thermally stable Re-rich phase remaining stationary, and a thermally instable Ni-rich phase diffusing around on the surface forming clusters. The supposition of phase separation is supported by Fig. S1† where it can be seen that the (100) and (002) reflections in the $Re_{55}Ni_{45}$ spectra are split into two peaks, while no peak splitting is observed in the $Re_{88}Ni_{12}$ spectra. We then evaluated the thermal stability of several Re-rich compositions, $Re_{63}Ni_{37}$, $Re_{80}Ni_{20}$ and $Re_{88}Ni_{12}$. Fig. 3d–f shows SEM images of these compositions after annealing at 1000 °C for 1 h, which further supports that the greater the Re content, the more thermally stable the scaffold. Although it may have been interesting to evaluate even greater Re content alloys, the very low faradaic efficiency (<10% for films with final Re content of >90%) during the fabrication of alloys lead to significant side reactions,[41] resulting in deposition of low quality materials.

The thermal stability of the $Re_{88}Ni_{12}$ scaffolds, the highest Re content consistently obtained in a high quality sample, was then investigated over longer annealing times. Shown in Fig. 4 are the SEM images after annealing at 1000 °C for Fig. 4a–c 1 h, Fig. 4d–f 5 h and Fig. 4g 10 h. Significant aspects of the microstructure remained past 5 h. From Fig. 4c and f, it is clear that grain growth and surface diffusion are both contributed to surface roughening and the degradation of the structure. After annealing for 10 h (Fig. 4g), the structure lost considerable structural integrity and appeared similar to the pure Ni sample annealed at 700 °C. Our material therefore presents not only the highest thermal stability compared to the list of previously reported electroplated refractory inverse opals (*i.e.* bulk material melting temperature higher than 1400 °C), but also outstanding properties relative to those prepared from other synthetic methods (Table S1, ESI†).

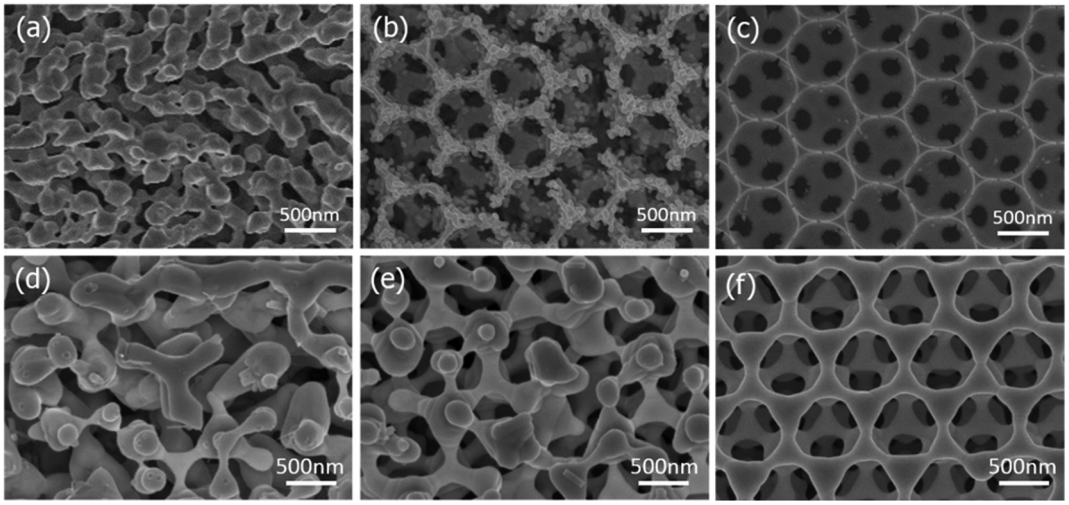

Fig. 3 SEM images of inverse opals after thermal annealing (a) Ni, (b) $Re_{55}Ni_{45}$, (c) $Re_{88}Ni_{12}$ at 700 °C for 1 h and (d) $Re_{63}Ni_{37}$, (e) $Re_{80}Ni_{20}$ and (f) $Re_{88}Ni_{12}$ at 1000 °C for 1 h. All annealing tests are conducted under forming gas. Sample compositions quantified by ICP.

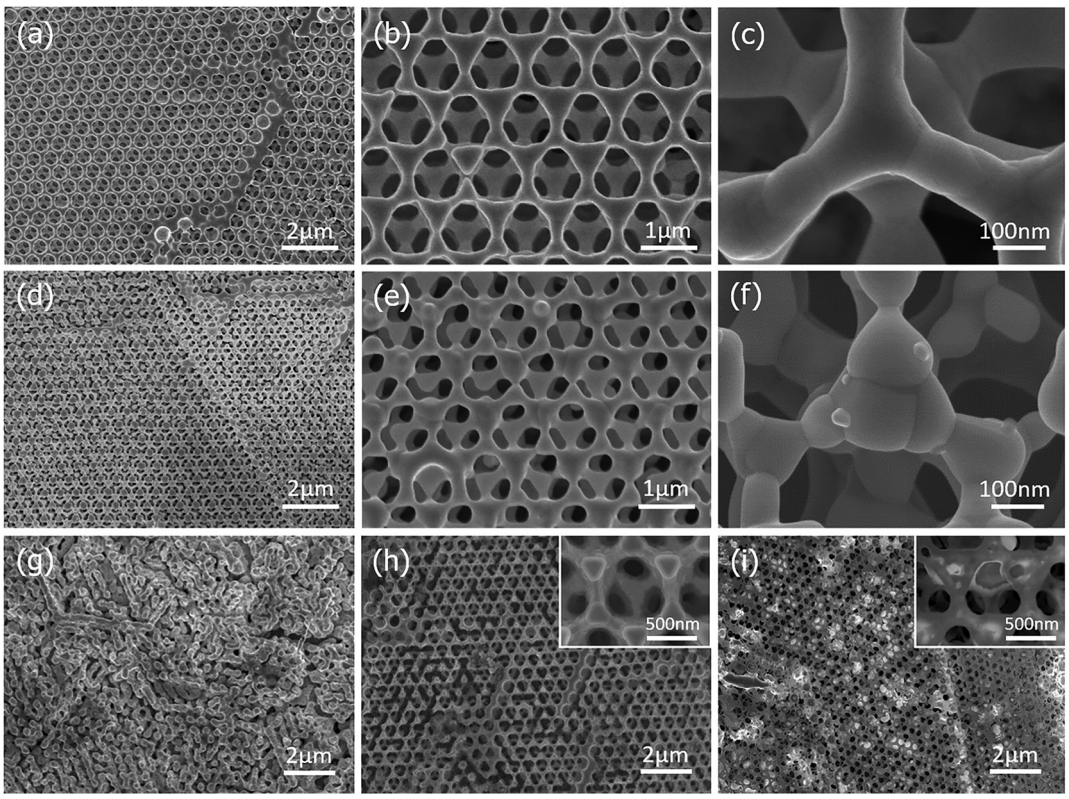

Fig. 4 SEM images of bare $Re_{88}Ni_{12}$ inverse opals after annealing at 1000 °C for (a)–(c) 1 h, (d)–(f) 5 h and (g) 10 h. Higher magnification images after annealing for 12 h at 1000 °C for $Re_{88}Ni_{12}$ inverse opals protected with (h) 25 nm Al_2O_3 and (i) 25 nm HfO_2.

To improve the thermal stability, a 25 nm thick Al_2O_3 or HfO_2 layer was conformally grown on the scaffold surface *via* atomic layer deposition (ALD). Fig. 4h and i present images of the Al_2O_3 and HfO_2 protected structures, respectively, after annealing at 1000 °C for 12 h. The Al_2O_3 coating leads to a clear stability improvement, in agreement with other reports where refractory ceramic coatings are used to slow down material remodeling processes.[25,26] However, the HfO_2 layer does not appear to protect the structure, in contrast with other reports that suggest HfO_2 would be a better protective coating than Al_2O_3 because of its higher melting temperature.[25] This may be caused by a reaction mechanism reported previously,[45]

where HfO_2 is reduced by Re in the presence of hydroxyl groups. Since our Re alloys are deposited from aqueous solution, there may be hydroxyl groups present.

As previously mentioned, refractory photonic crystals (PhCs) have been suggested as spectrally-selective emitter elements for thermophotovoltaic energy harvesting systems.[24,25] Because of their thermal stability, ReNi PhCs could be interesting for such an application. To gain an understanding for the potential of ReNi PhCs, the reflectance spectra of our ReNi inverse opals are both simulated using Lumerical FDTD, and characterized using FTIR. Fig. 5 summarizes the simulated and experimental data. Since our material is nearly 90 at% Re, the optical constants for pure Re are adopted here for the simulation.[46] Shown in Fig. 5a are reflectance simulations for structures with air sphere diameters of 600 nm, 1000 nm and 1400 nm. The simulations are internally consistent, with an air-sphere size dependent transition between a high reflectivity at longer wavelengths (longer than ~4 μm) and a low reflectivity at shorter wavelengths. Shown in Fig. 5b are reflectance spectra measured from the $Re_{88}Ni_{12}$ inverse opals made using 1000 nm diameter PS spheres as well as the 1000 nm air-sphere simulation from Fig. 5a for comparison. The reflectance from the as-deposited samples agrees well with the simulation, with only a slightly lowered reflectivity at longer wavelengths. A 5% to 10% decrease in reflectivity is observed after annealing the sample at 1000 °C for 1 h, however, the shape of the reflectivity curve is maintained. Annealing of the same sample under 1000 °C for an additional 5 h reduces the reflectivity further. As observed in the SEM images (Fig. 4), after 1 h at 1000 °C the structure is relatively intact, while after 5 h, there is significant structural degradation.

We evaluated the mechanical property of the ReNi inverse opals using a Berkovich indentation tip (see Fig. S2, ESI,† for the representative sample morphology after indentation). To ensure sufficient contact area between the tip and the sample, while avoiding substrate-induced artifacts due to excessive compression of the scaffold, a maximum load of 3.5 mN is used, and the maximum indentation depth is set to ~600 nm which is less than 10% of the total sample thickness. To minimize sample-to-sample variation, both a pure Ni inverse opal and a $Re_{88}Ni_{12}$ inverse opal are prepared from two equivalent pieces of polystyrene opal templates originating from a single larger piece, guaranteeing the two opals contain the same microstructure. The electroplated Ni and ReNi samples were then cropped into two equivalent pieces with one piece

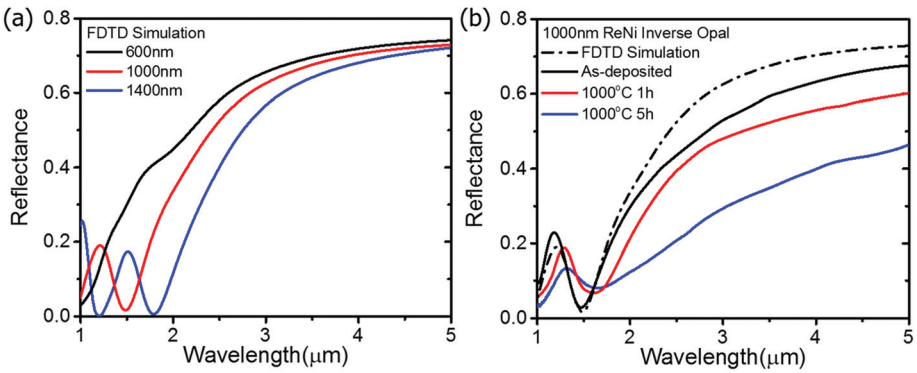

Fig. 5 (a) FDTD reflectance simulations of Re inverse opals containing 600 nm, 1000 nm and 1400 nm diameter air spheres. (b) FTIR measured (solid lines) reflectances of a $Re_{88}Ni_{12}$ inverse opal templated by 1000 nm spheres as-deposited, and after annealing at 1000 °C for 1 h and 5 h. The 1000 nm simulation from (a) is included on (b) (dot-dashed line).

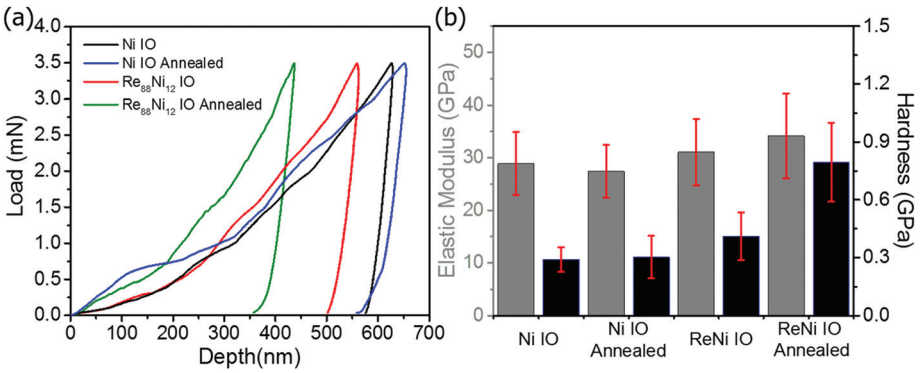

Fig. 6 Mechanical properties of Ni and $Re_{88}Ni_{12}$ inverse opals (as deposited and after annealing at 500 °C for 10 h) (a) typical load displacement nanoindentation curves and (b) elastic modulus (*E*) and hardness (*H*) averaged over 20 measurements. Error bars are one standard deviation.

annealed at 500 °C, and the other not. The metal filling fraction of the porous scaffold is estimated to be about 20% using a method previously discussed in the literature.[12] Fig. 6a shows the load *vs.* displacement curves for the two sets of samples under different thermal treatment conditions. The elastic modulus (E) and hardness (H) of the four inverse opals, averaged over 20 indents each, are summarized in Fig. 6b. The pure Ni sample exhibited an E of 28 ± 6 GPa and H of 0.30 ± 0.08 GPa, the as-deposited $Re_{88}Ni_{12}$ sample exhibited an E of 31.07 ± 6.32 GPa and H of 0.41 ± 0.12 GPa. While there are no clear differences in the mechanical properties of the annealed and unannealed Ni inverse opals, for the $Re_{88}Ni_{12}$ sample, after annealing, E increased to 35.15 ± 8.03 GPa, and H nearly doubled to 0.79 ± 0.24 GPa. Table S2 in the ESI† shows the hardness of the annealed $Re_{88}Ni_{12}$ sample is about 1.4× higher than the hardness of previously reported SiC inverse opals which at that time was the greatest hardness measured for an inverse opal.[47] We suspect that the improvement in mechanical properties were resulted from both material densification after annealing and the reduction of hydrogen embrittlement by driving hydrogen out of the structure, a problem frequently seen in electrodeposited metals that leads to reduced ductility.[43]

Conclusion

Here we report the first ReNi alloy inverse opals formed by electrodeposition through self-assembled polystyrene sacrificial opal templates. The resulting Re-rich three-dimensionally microstructured materials contain a periodic internal pore structure, and are thermally stable up to 1000 °C for several hours, exceeding the thermal stability of all previously electrodeposited inverse opals. In addition to the excellent thermal properties, the structures exhibit an ~60% modulation in reflectivity between 1 and 5 μm, even after annealing under 1000 °C, which may make such materials interesting as refractory optical elements. The pronounced high strength and toughness, outstanding thermal stability, as well as the ease by which the Re and Ni composition can be adjusted may also enable these structures to find use in high temperature mechanical applications including actuators or filtration,[48,49] and 3D scaffolds for high temperature material synthesis (*e.g.* CVD graphene synthesis[50]) and high temperature catalysis.[51]

Experimental methods

Opal template assembly

3D face-centered cubic opals are made by self-assembly of polystyrene (PS) colloids (ThermoFisher Scientific Inc.) *via* evaporation. 0.6 g of colloids are first well dispersed in 45 ml of Millipore water by sonication. W foil, the substrate used here, is cleaned by sonication in acetone, isopropanol alcohol (IPA), and DI water for 15 min each, before use. The W foil substrates are then placed vertically within vials containing the colloidal dispersion, and placed in an incubator at 55 °C driving water evaporation and thus opal formation. The resulting opal template is then sintered at 95 °C for 2 hours to strengthen the opal and increase the contact area of the spheres (which will become the connection between the voids in the templated metal foam).

ReNi inverse opal growth

The electroplating solution used in this work is adapted from earlier reported works.[41,42] Ammonium perrhenate (NH_4ReO_4 ≥ 99%, 316954 Sigma Aldrich) is used as the Re precursor and nickel(II) sulfamate tetrahydrate ($Ni(SO_3NH_2)_2{\cdot}H_2O$ 98%, 262277 Sigma Aldrich) as the Ni precursor. Citric acid and NaOH are used as the complexing agent and pH adjusting agent, respectively. All electrolytes in this work are controlled to have a pH 6 ± 0.1. A concentration variation of 34–93 mM NH_4ReO_4, 34–120 mM $Ni(SO_3NH_2)_2$ are used depending on the need for obtaining different fractions of Re and Ni in the alloy. As one example, 93 mM NH_4ReO_4 and 93 mM $Ni(SO_3NH_2)_2$ is used for getting the high Re concentration of ~88 at%. A three-electrode electrodeposition setup is used. The working electrode (cathode) is connected to the conductive substrate, Pt foil is used as the counter electrode (anode), and the deposition voltage is held near −0.77 volts *vs.* the Ag/AgCl reference electrode. The reference Ni IO is electrodeposited through the opal at a constant current density of 5 mA cm^{-2} in a Technic RTU Mechanical Agitation commercial solution. After the ReNi or Ni deposition is complete, the samples are immersed in THF overnight to dissolve the PS template.

Material characterization

Imaging is performed using a Hitachi S-4800 SEM. Energy dispersive X-ray spectroscopy (EDX) is collected using an Oxford Instruments ISIS EDS X-ray Microanalysis System using an accelerating voltage of 15 keV. X-ray diffraction (XRD) is collected with a Philips X'Pert MRD system, using Cu K_α radiation (0.15418 nm), and a scan rate of 0.5° min^{-1}. A Hysitron Triboindentor with a Berkvich tip is used to measure samples' elastic modulus (E) and hardness (H).

Thermal annealing

Thermal annealing studies are conducted in a Thermo Scientific tube furnace equipped with a quartz tube. Samples are placed in ceramic crucibles. The tube is typically purged with ultra-high purity forming gas (5% H_2, 95% Ar) for at least 30 min before annealing. The temperature ramp rate is set to 5 °C min^{-1}. Forming gas (5% H_2 in Ar) is used for all thermal annealing experiments to provide a reducing atmosphere.

Optical characterization

Simulations on the ReNi IOs are carried out using Lumerical FDTD software. The optical constants for Re are obtained from the literature.[46] A Vertex 70 FTIR with a Bruker Hyperion microscope attachment is used for taking the reflectance spectrum from ReNi IO samples. The data, for all wavelengths, are collected using a 15× CaF_2 objective, a CaF_2 beam splitter and a liquid nitrogen-cooled InSb detector.

Conflicts of interest

There are no conflicts of interest to declare.

Acknowledgements

This work was supported by the U.S. Department of Energy "Light Material Interactions in Energy Conversion" Energy Frontier Research Center under grant DE-SC0001293 (optical measurements and sample fabrication). This research was carried out in part in the Center for Microanalysis of Materials in the Frederick Seitz Materials Research Laboratory at the University of Illinois.

References

1 M. F. Ashby, A. Evans, N. A. Fleck, L. J. Gibson, J. W. Hutchinson and H. N. Wadley, *Mater. Des.*, 2002, **23**, 119.
2 J. Banhart, *Prog. Mater. Sci.*, 2001, **46**, 559–632.
3 G. J. Davies and S. Zhen, *J. Mater. Sci.*, 1983, **18**, 1899–1911.
4 T. A. Schaedler, A. J. Jacobsen, A. Torrents, A. E. Sorensen, J. Lian, J. R. Greer, L. Valdevit and W. B. Carter, *Science*, 2011, **334**, 962–965.
5 L. R. Meza, S. Das and J. R. Greer, *Science*, 2014, **345**, 1322–1326.
6 Q. Zheng, H. Kim, R. Zhang, M. Sardela, J. Zuo, M. Balaji, S. Lourdudoss, Y.-T. Sun and P. V. Braun, *J. Appl. Phys.*, 2015, **118**, 224303.
7 H. Ning, J. H. Pikul, R. Zhang, X. Li, S. Xu, J. Wang, J. A. Rogers, W. P. King and P. V. Braun, *Proc. Natl. Acad. Sci. U. S. A.*, 2015, **112**, 6573–6578.
8 R. Zhang, H. Ning, N. A. Krueger, D. Bacon-Brown and P. V. Braun, *Adv. Opt. Mater.*, 2016, **4**, 1533–1540.
9 M. Deubel, G. von Freymann, M. Wegener, S. Pereira, K. Busch and C. M. Soukoulis, *Nat. Mater.*, 2004, **3**, 444–447.
10 J. Baumeister, J. Banhart and M. Weber, *Mater. Des.*, 1997, **18**, 217–220.
11 H. Zhang and P. V. Braun, *Nano Lett.*, 2012, **12**, 2778–2783.
12 H. Zhang, X. Yu and P. V. Braun, *Nat. Nanotechnol.*, 2011, **6**, 277–281.
13 S. Guldin, S. Hüttner, M. Kolle, M. E. Welland, P. Müller-Buschbaum, R. H. Friend, U. Steiner and N. Tétreault, *Nano Lett.*, 2010, **10**, 2303–2309.
14 D. Zhou and R. Biswas, *J. Appl. Phys.*, 2008, **103**, 93102.
15 G. Collins, M. Blömker, M. Osiak, J. D. Holmes, M. Bredol and C. O'Dwyer, *Chem. Mater.*, 2013, **25**, 4312–4320.
16 J.-S. Yu, S. Kang, S. B. Yoon and G. Chai, *J. Am. Chem. Soc.*, 2002, **124**, 9382–9383.
17 J. Zhang and W. Liu, *J. Membr. Sci.*, 2011, **371**, 197–210.
18 K. Aydin, V. E. Ferry, R. M. Briggs and H. A. Atwater, *Nat. Commun.*, 2011, **2**, 517.
19 I. El-Kady, M. M. Sigalas, R. Biswas, K. M. Ho and C. M. Soukoulis, *Phys. Rev. B: Condens. Matter*, 2000, **62**, 15299.
20 J. G. Fleming, S. Y. Lin, I. El-Kady, R. Biswas and K. M. Ho, *Nature*, 2002, **417**, 52–55.
21 B. Luk'yanchuk, N. I. Zheludev, S. A. Maier, N. J. Halas, P. Nordlander, H. Giessen and C. T. Chong, *Nat. Mater.*, 2010, **9**, 707–715.
22 I. Celanovic, F. O'Sullivan, N. Jovanovic, M. Qi and J. G. Kassakian, in *Photonics Europe*, International Society for Optics and Photonics, 2004, pp. 416–422.
23 P. Nagpal, S. E. Han, A. Stein and D. J. Norris, *Nano Lett.*, 2008, **8**, 3238–3243.
24 V. Rinnerbauer, S. Ndao, Y. X. Yeng, W. R. Chan, J. J. Senkevich, J. D. Joannopoulos, M. Soljačić and I. Celanovic, *Energy Environ. Sci.*, 2012, **5**, 8815.
25 K. A. Arpin, M. D. Losego, A. N. Cloud, H. Ning, J. Mallek, N. P. Sergeant, L. Zhu, Z. Yu, B. Kalanyan, G. N. Parsons, G. S. Girolami, J. R. Abelson, S. Fan and P. V. Braun, *Nat. Commun.*, 2013, **4**, 2630.
26 K. A. Arpin, M. D. Losego and P. V. Braun, *Chem. Mater.*, 2011, **23**, 4783–4788.
27 Z. Wang, F. Li, N. S. Ergang and A. Stein, *Chem. Mater.*, 2006, **18**, 5543–5553.
28 P. Nagpal, D. P. Josephson, N. R. Denny, J. DeWilde, D. J. Norris and A. Stein, *J. Mater. Chem.*, 2011, **21**, 10836.
29 W. S. Williams, *JOM*, 1998, **50**, 62–66.
30 E. W. Bohannan, M. G. Shumsky and J. A. Switzer, *Chem. Mater.*, 1999, **11**, 2289–2291.
31 O.-H. Kim, Y.-H. Cho, S. H. Kang, H.-Y. Park, M. Kim, J. W. Lim, D. Y. Chung, M. J. Lee, H. Choe and Y.-E. Sung, *Nat. Commun.*, 2013, **4**, 2473.
32 J. Wang, H. Zhou, J. Nanda and P. V. Braun, *Chem. Mater.*, 2015, **27**, 2803–2811.
33 A. Ispas, B. Adolphi, A. Bund and F. Endres, *Phys. Chem. Chem. Phys.*, 2010, **12**, 1793–1803.
34 E. Lassner and W.-D. Schubert, *Tungsten*, Springer US, Boston, MA, 1999.
35 P. Kofstad, *J. Electrochem. Soc.*, 1963, **110**, 491–501.
36 G. Rouschias, *Chem. Rev.*, 1974, **74**, 531–566.
37 A. F. Giamei and D. L. Anton, *Metall. Trans. A*, 1985, **16**, 1997–2005.
38 N. S. Jacobson, D. L. Myers, D. Zhu and D. L. Humphrey, *Oxid. Met.*, 2001, **55**, 471–480.
39 T. M. Pollock and S. Tin, *J. Propul. Power*, 2006, **22**, 361–374.
40 R. Burch, *Platinum Met. Rev.*, 1978, **22**, 57–60.
41 A. Naor, N. Eliaz and E. Gileadi, *Electrochim. Acta*, 2009, **54**, 6028–6035.
42 A. Naor, N. Eliaz and E. Gileadi, *J. Electrochem. Soc.*, 2010, **157**, D422.
43 D. R. Gabe, *J. Appl. Electrochem.*, 1997, **27**, 908–915.
44 H. Okamoto, *J. Phase Equilib. Diffus.*, 2012, **33**, 346–346.
45 M. Copel, R. P. Pezzi, D. Neumayer and P. Jamison, *Appl. Phys. Lett.*, 2006, **88**, 72914.

46 E. D. Palik, *Handbook of optical constants of solids*, Academic press, 1998, vol. 3.
47 J. Zhou, H. Li, L. Ye, J. Liu, J. Wang, T. Zhao, L. Jiang and Y. Song, *J. Phys. Chem. C*, 2010, **114**, 22303–22308.
48 W. Peukert, *Filtr. Sep.*, 1998, **35**, 461–464.
49 L.-P. Lefebvre, J. Banhart and D. C. Dunand, *Adv. Eng. Mater.*, 2008, **10**, 775–787.
50 Y. Zhang, L. Zhang and C. Zhou, *Acc. Chem. Res.*, 2013, **46**, 2329–2339.
51 A. J. Zarur and J. Y. Ying, *Nature*, 2000, **403**, 65–67.